*CANCER BIOTHERAPY & RADIOPHARMACEUTICALS*
Volume 23, Number 4, 2008

DOI: 10.1089/cbr.2007.0457

# Quantitative Serial Imaging of an $^{124}$I Anti-CEA Monoclonal Antibody in Tumor-Bearing Mice

**James R. Bading,[1] Magnus Hörling,[2] Lawrence E. Williams,[3] David Colcher,[1]**
**Andrew Raubitschek,[1] and Sven E. Strand[2]**
Departments of [1]Radioimmunotherapy, [3]Radiology, City of Hope, Duarte, CA
[2]Department of Medical Radiation Physics, Lund University, Lund, Sweden

## *ABSTRACT*

***Objective:*** *The 4.2-day half-life of $^{124}$I favors its use for positron emission tomography (PET) of monoclonal antibodies (mAbs). However, high positron energy and $\beta^+$-associated cascade $\gamma$ rays pose image resolution and background noise problems for $^{124}$I. This study evaluated quantitative PET of an $^{124}$I mAb in tumor-bearing mice.* ***Methods:*** *An R4 microPET™ (Siemens/CTIMI, Knoxville, TN) was used with standard energy and coincidence timing windows (350–750 keV and 6 ns, respectively), delayed random coincidence subtraction, iterative image reconstruction, and no attenuation or scatter correction. Image resolution, contrast, and response linearity were compared for $^{124}$I and $^{18}$F, using phantoms. Nude mice bearing human colon tumors (LS-174T) were injected intravenously with a chimeric $^{124}$I anti-CEA mAb (cT84.66) and imaged serially 1 hour to 7 days postinjection. Venous blood was sampled to validate image-derived blood curves. Mice were sacrificed after the final scan, and the biodistribution of $^{124}$I was measured by direct tissue assay. Images were converted to units of kBq/g for each tissue of interest by comparing the final scans with the direct assays.* ***Results:*** *Measured resolution (FWHM) 0–16 mm from the scanner axis was 2.3–2.7 mm for $^{124}$I versus 1.9–2.0 mm for $^{18}$F. Due to true coincidence events between annihilation photons and cascade $\gamma$ rays, background was greater for $^{124}$I than $^{18}$F, but the signal-to-background ratio was still more than 20, and $^{124}$I image intensities varied linearly with activity concentration. Tissue-based calibration worked well (i.e., PET blood curves agreed with direct measurements within 12% at all time points), while calibration, based on a cylindrical phantom approximating the mouse body, yielded tumor quantitation that was 46%–66% low, compared with direct assay.* ***Conclusions:*** *Images of quantitative accuracy sufficient for biodistribution measurements can be obtained from tumor-bearing mice by using $^{124}$I anti-CEA mAbs with standard microPET acquisition and processing techniques, provided the calibration is based on the direct assay of excised tissue samples.*

**Key words:** antibody, cancer, molecular imaging, PET, radioimmunotherapy

## INTRODUCTION

Radiotracer imaging is used to measure the biodistribution of tumor-targeted monoclonal antibodies (mAbs) in radioimmunotherapy (RIT), primarily for the purpose of estimating absorbed doses to normal tissues and organs as well as tumors. When the radionuclide is $^{131}$I, external imaging can be performed directly on the therapeutic mAbs.[1] When the therapeutic nuclide is $^{90}$Y (a radiometal that emits only $\beta^-$ particles), imaging is commonly performed by using $^{111}$In as a surrogate radiolabel.[2] Typically, imaging is performed during the week preceding the administration of the RIT activity and may be repeated after coadministering the imaging mAb

---

***Address reprint requests to:** James R. Bading; Department of Radioimmunotherapy, City of Hope; 1500 Duarte Road, Duarte, CA 91010-3000; Tel.: 626-256-4673, ext. 63904; Fax: 626-301-8817*
***E-mail:*** **jbading@coh.org**

with the therapeutic activity. Planar, conjugate-view, whole-body imaging is performed on a semidaily basis for as many as 7 days. The recent availability of in-line combination computed tomography (CT) and single-photon emission computed tomography (SPECT) scanners has facilitated the use of attenuation-corrected SPECT to supplement planar scanning in an effort to improve the estimation of radiolabel activity concentration in structures superimposed in the two-dimensional (2D) planar images.[3]

Positron emission tomography (PET) has major advantages over SPECT for *in vivo* measurement of tissue-activity concentration because of its better spatial resolution, higher sensitivity, and more accurate attenuation correction. The primary limitation for PET in RIT has been a lack of $\beta^+$-emitting isotopes with half-life and chemical labeling properties suitable for use with mAbs. Iodine-124 is a $\beta^+$-emitter that satisfies both criteria (i.e., its half-life [4.2 days]) is well matched to the biodistribution dynamics of intact mAbs, and labeling of biomolecules with iodine is a well-known, relatively facile process. Further, $^{124}$I is potentially important as an imaging surrogate for $^{131}$I, which is widely used as a therapeutic isotope in RIT. Another advantage of $^{124}$I is that its relatively long half-life allows the use of activity produced by a remote radionuclide production facility, thus eliminating the need for an on-site cyclotron.

Iodine-124 has a complex decay scheme.[4] Two positron-emitting transitions have significant probability, but the combined abundance of these is only 23%, compared, for example, to the 97% $\beta^+$ yield of $^{18}$F. The positrons emitted by $^{124}$I are also of higher energy ($E_{max} = 1.5$ and 2.1 MeV) than those emitted by $^{18}$F ($E_{max} = 0.6$ MeV). This translates to $\beta^+$ root-mean-square ranges in water of approximately 0.8 and 1.3 mm for $^{124}$I, compared with 0.2 mm for $^{18}$F, and thus may cause a significant loss of spatial resolution for small-animal PET, where intrinsic resolution is on the order of 1–2 mm.

In addition to positrons, $^{124}$I also emits $\gamma$ rays at many different energies (more than 90 possible transitions), resulting in increased random coincidence counts in PET. A potentially worse problem is that approximately 50% of the $\beta^+$s are emitted in cascade with a 603-keV $\gamma$ ray. This causes another complication due to erroneous events in which a $\gamma$ ray is detected in true coincidence with one of the annihilation photons. (Such events will be referred to as "true-coincidence $\gamma$ ray background"). Because the direction of the 603-keV $\gamma$-ray emission has no correlation with those of the annihilation photons, the recorded lines of response from such events provide no information about the activity distribution within the studied object.

Another potential problem with the use of $^{124}$I for imaging in RIT is the tendency for iodine to be lost from the injected mAb and released into the circulation, an event that happens most often following cellular incorporation and metabolic breakdown of the mAb. This may occur in normal tissues and organs (especially the liver) as well as in tumors, and it may seriously obscure image interpretation. The current study utilized mAbs against CEA (carcinoembryonic antigen), which is often highly expressed in carcinomas of the colon, breast, and lung.[5] Deiodination may be minimal for $^{124}$I-labeled anti-CEA mAbs, because anti-CEA mAbs are not strongly internalized after binding to CEA on cell surfaces.[6]

Iodine-124 has been used with clinical[7–9] and small-animal[10–12] PET scanners to visualize mAbs (or engineered fragments) in tumor-xenografted mice. There have been a few reports on the physics of $^{124}$I imaging with small-animal scanners[13,14] and several studies in which small animal PET scanners were used to measure activity concentrations of $^{124}$I-labeled tracers in tumors and nontumor tissues/organs.[12,15,16] To our knowledge, validation of quantitative imaging with $^{124}$I in mice using a small-animal PET scanner has not been previously reported.

The overall aim of this study was to acquire knowledge and understanding of how the properties of $^{124}$I affect image quality and quantitation in small-animal PET. In particular, an effort was made to characterize the quantitative accuracy and assess the practical utility of small-animal PET imaging with $^{124}$I for pharmacokinetic characterization in preclinical RIT research with tumor-bearing mice.

## METHODS

### Radiotracers

Human/murine chimeric T84.66, an anti-CEA intact $IgG_1$ with high affinity (affinity constant $= 1 \times 10^{11}\ M^{-1}$)[17] and specificity for CEA, was prepared according to published methods,[18] and labeled with $^{124}$I, using the iodogen method.[19] Iodine-124 was obtained as NaI (radiochemical purity greater than 95%, radionuclidic purity greater than 99.9% at initial calibration) from IBA/Eastern Isotopes (Sterling, VA). The radiolabeled antibody was separated from unincorporated $^{124}$I by size-exclusion chromatography. The peak was shown to be 100% protein-bound $^{124}$I by instant thin-layer chromatography (ITLC) and high-performance liquid chromatography (HPLC). Immunoreactivity was measured in an HPLC shift assay; 100% of the radiolabeled antibody shifted to a higher molecular weight when a 20-fold excess of antigen was added. Fluorine-18 was purchased from Cardinal Health, Van Nuys, CA.

### Mouse Model

Human colon carcinoma cells (LS-174T) were purchased from ATCC (Manassas, VA) and maintained by serial passage in our laboratory. Female athymic nude mice were obtained from Charles River Laboratories (Wilmington, MA). At age 7–8 weeks, the mice were implanted subcutaneously in the right flank with $1.5 \times 10^6$ LS-174T cells. Imaging experiments were started 10 days postimplant, when the tumors had reached several millimeters in diameter. Imaging, blood sampling, and sacrifice procedures were performed under inhalation anesthesia, using isoflurane (IsoFlo; Abbot Animal Health, Chicago, IL). All procedures were conducted according to a protocol approved by the Research Animal Care Committee at City of Hope (Duarte CA) and adhered to national guidelines on the care and use of laboratory animals.

### Imaging Experiments

Studies were conducted using a microPET™ Model R4 small-animal PET scanner (Siemens/CTIMI, Knoxville, TN). The performance of the microPET R4 has been thoroughly evaluated, although primarily with $^{18}$F.[20] Standard techniques were used to acquire the microPET images. In particular, the standard energy window (350–750 keV) and coincidence timing window (6 ns) were employed throughout. All data were acquired in list mode. The data were corrected for radionuclide decay to the time at which the scan was initiated, as well as for dead-time loss. Random coincidence events were subtracted from the raw data by using the delayed window method. Although the system is capable of attenuation and scatter corrections, these were not employed, in part because the scatter correction does not address the problem of true-coincidence $\gamma$-ray background events obtained with $^{124}$I.

All data acquisition, histogramming, and reconstruction tasks were done with the Visual C++ based user interface microPET Manager™. List mode data were rebinned and histogrammed into three-dimensional (3D) sinograms, using a span of 3 and a ring difference of 31. For phantom studies, three different reconstruction algorithms were used. The first was a standard 2D ordered subsets expectation maximization (OSEM) algorithm incorporating Fourier rebinning and using four iterations of 16 subsets.[21] The OSEM algorithm models the Poisson distribution of coincidence data but not the physics of camera response. The second reconstruction program employed 3D OSEM (two iterations, 12 subsets), followed by a maximum *a posteriori* (MAP) algorithm (18 iterations).[22] The combined algorithm is referred to in this paper simply as "MAP." In addition to the Poisson distribution of coincidence data, the MAP algorithm accounts for annihilation photon noncolinearity and misplacement of coincidence events due to oblique incidence of photons on detectors. The algorithm does not, however, correct for $\beta^+$ range and thus is more appropriate for $^{18}$F than for $^{124}$I. The smoothing parameter for MAP was set to 0.01, and the option of uniform spatial resolution was selected. Images from the resolution phantom were also reconstructed by 3D-filtered backprojection (3DRP).[23] When it turned out that resolution was substantially worsened, compared with the iterative techniques (see below), no further use was made of 3DRP. Image matrix size for all reconstructions was $128 \times 128 \times 63$ voxels, with voxel dimensions of $0.85 \times 0.85 \times 1.3$ mm (voxel volume, 0.93 mm$^3$). Image reconstruction times on the microPET console (Dell PWS 651, single 3.1 GHz CPU, 2 GByte RAM) were 40 seconds, 26 minutes, and 5 minutes, respectively for OSEM, MAP, and 3DRP. The *in vivo* studies were reconstructed by using both the MAP and OSEM algorithms.

Images were calibrated in units of absolute activity concentration by scanning a 20-mm diameter cylinder (24-cc plastic counting vial) containing known activity concentrations of $^{124}$I or $^{18}$F. [Calibration factor = phantom activity concentration (kBq/cc)/average image intensity (proportional to mean count rate per voxel; proprietary units for microPET) for a volume of interest (VOI) drawn within the central region of the phantom image.] For PET imaging of

[$^{124}$I]cT84.66 in mice, separate image calibration factors were also determined for tumor, blood (heart), and liver by comparing the final scans with direct assays of tissues and organs performed after the animals were sacrificed. For a given tissue or organ, the calibration factor was computed as directly measured activity concentration (kBq/g)/average image intensity for a VOI drawn on the microPET image of the tissue or organ.

The imaging characteristics of $^{124}$I and $^{18}$F were evaluated by using three different phantoms. A resolution phantom was configured by using three isotope-filled capillary tubes (glass, 1 mm internal diameter) mounted through two Styrofoam blocks at 0, 8, and 16 mm off center and housed in a water-filled plastic laboratory jar 40 mm in diameter. A response linearity phantom was formed by filling four plastic tuberculin syringes (1 cc, 5 mm internal diameter) with four different, known activity concentrations (15–900 kBq/cc), then mounting them 90 degrees apart and 10 mm off center through a machined Plexiglas cylinder (diameter 35 mm, length 63 mm) to simulate attenuation and scatter within the body of a mouse. Image contrast, scatter, and true-coincidence $\gamma$-ray background were assessed with a water-filled plastic microcentrifuge vial (0.7 cc) attached to the cap of a 24-cc plastic scintillation tube with Velcro and immersed in a volume of radionuclide-containing water sufficient to fill the tube outside the vial (Fig. 1).

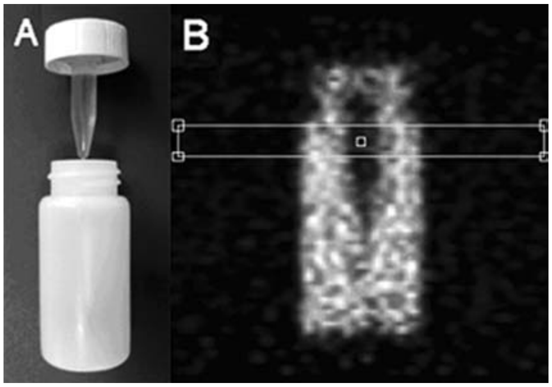

**Figure 1.** Contrast phantom. (**A**) Photo of the phantom. (**B**) Coronal positron emission tomography (PET) image slice (maximum *a posteriori* reconstruction) through the phantom loaded with $^{124}$I (90 kBq/mL) showing a profile window positioned over the part including the nonradioactive, water-filled insert. Scan duration was 30 minutes. Phantom dimensions (height × diameter in mm): outer vial 60 × 26, inner vial 30 × 7.

Two (2) mice (23 and 26 g) were injected via the tail vein with $^{124}$I anti-CEA cT84.66 mAb (administered activity and protein approximately 70 kBq/g and 0.3 $\mu$g/g, respectively). At 1, 4, 21, 45, 69, 141, and 165 hours postinjection, the mice were anesthetized with isoflurane, placed prone on a thin cardboard platform, positioned tailfirst in the microPET, and scanned. Scan duration was 20 minutes for the first three time points, 30 minutes for the fourth and fifth time points, and 40 minutes for the last two time points. For direct assay of blood activity concentration, a blood sample (approximately 10 $\mu$L, exact volume determined by measuring blood column length) was obtained via tail prick and a calibrated capillary tube just before and just after each scan. (The mean values of the before-and-after samples were used for comparison with PET images of the heart for the corresponding time points.) After completion of the last scan, a final blood sample was taken by trans-thorax aspiration, the mice were sacrificed, and livers and tumors were harvested. Tissue samples, including blood, were weighed and assayed for $^{124}$I activity, using a calibrated gamma counter (Model 1480 Wizard 3″; Wallac Oy, Turku, Finland).

Image viewing and analysis were done by using the IDL (Interactive Data Language; Research Systems Inc. Boulder, CO)-based analysis software, ASIPro™, which is provided with the microPET scanner. This program contains a profile tool as well as tools for creating VOIs. The strategy used for VOI definitions in mice varied among different tissues and organs. For tumors, the lower threshold for a 3D region-grow algorithm was adjusted to identify and obtain average intensities for the four hottest voxels, not necessarily all of which were in the same slice. For the heart, the region-grow algorithm was used to identify and average over voxels having intensities within 70% of the maximum voxel. Liver was not clearly delineated in the images. Thus, VOIs were hand drawn within what was assumed to be the liver on each of three consecutive slices lying between the heart and stomach. Liver VOIs were drawn so as to minimize contributions from large vessels.

Time-activity curves (TACs) were evaluated for tumors, blood, and liver. The curves were decay corrected to time of injection and calibrated individually in units of percentage injected dose/g tissue by normalizing the VOI-derived average image intensities of the final image sets to the activity concentrations measured directly in the corresponding tissue and organ samples following the final scan. Curve amplitudes at earlier scan times were determined by the relative decay-corrected image intensities of the tissues and organs. In other words, absolute activity concentration (expressed as a percentage of injected activity) was determined by comparison with the direct assay, whereas microPET provided the TAC shapes.

## RESULTS

Findings of the spatial resolution study are summarized in Figure 2 and Table 1. The measured line source image full width at half maximum (FWHM) was 0.3–1.2 mm greater for $^{124}$I than $^{18}$F, presumably reflecting the difference in positron range. A somewhat better, spatially more uniform resolution was obtained with MAP, as compared with OSEM reconstruction, whereas

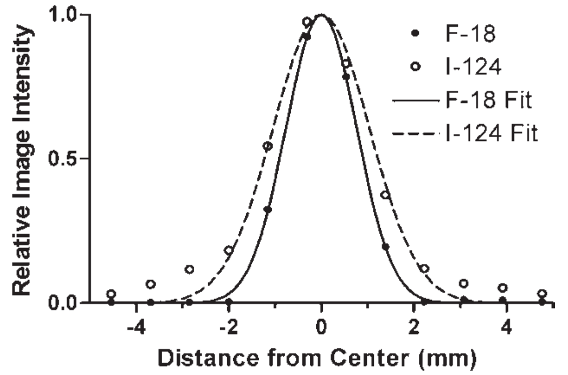

**Figure 2.** Spatial resolution results. Shown are the mean profiles (horizontal and vertical) of 10 consecutive transaxial image slices (maximum *a posteriori* reconstruction) of a line source positioned approximately in the center of the microPET transaxial field of view. Fitted Gaussian functions are superimposed on the data. Full width at half maximum is 1.9 mm for $^{18}$F, and 2.6 mm for $^{124}$I. The higher amplitude tails for $^{124}$I reflect the true-coincidence $\gamma$-ray background.

**Table 1.** Resolution of Reconstructed microPET Images[a]

| *Reconstruction method* | *Distance from scanner axis (mm)* | *Full width at half maximum (mm)* | | *Full width at tenth maximum (mm)* | |
|---|---|---|---|---|---|
| | | *radial* | *tangential* | *radial* | *tangential* |
| $^{18}$F | | | | | |
| OSEM | 0 | 1.84 ± 0.02[b] | | 3.49 ± 0.05[c] | |
| | 8 | 2.05 ± 0.06[c] | 1.94 ± 0.04[c] | 3.69 ± 0.08[d] | 3.56 ± 0.07[d] |
| | 16 | 2.10 ± 0.05[c] | 1.91 ± 0.03[c] | 3.89 ± 0.08[d] | 3.60 ± 0.07[d] |
| MAP | 0 | 1.88 ± 0.01[b] | | 3.52 ± 0.02[c] | |
| | 8 | 2.01 ± 0.02[c] | 1.99 ± 0.02[c] | 3.71 ± 0.02[d] | 3.69 ± 0.02[d] |
| | 16 | 1.89 ± 0.01[c] | 1.92 ± 0.03[c] | 3.53 ± 0.02[d] | 3.59 ± 0.03[d] |
| 3DRP | 0 | 2.47 ± 0.02[b] | | 4.59 ± 0.04[c] | |
| | 8 | 2.36 ± 0.03[c] | 2.59 ± 0.03[c] | 4.37 ± 0.03[d] | 4.76 ± 0.04[d] |
| | 16 | 2.51 ± 0.02[c] | 2.42 ± 0.02[c] | 4.63 ± 0.03[d] | 4.50 ± 0.03[d] |
| $^{124}$I | | | | | |
| OSEM | 0 | 3.00 ± 0.06[b] | | 6.07 ± 0.33[c] | |
| | 8 | 2.45 ± 0.17[c] | 2.33 ± 0.04[c] | 5.22 ± 0.28[d] | 5.30 ± 0.53[d] |
| | 16 | 2.97 ± 0.10[c] | 3.01 ± 0.03[c] | 5.92 ± 0.17[d] | 5.54 ± 0.35[d] |
| MAP | 0 | 2.62 ± 0.06[b] | | 5.16 ± 0.17[c] | |
| | 8 | 2.37 ± 0.15[c] | 2.25 ± 0.12[c] | 5.08 ± 0.81[d] | 5.40 ± 0.54[d] |
| | 16 | 2.35 ± 0.05[c] | 2.67 ± 0.12[c] | 4.92 ± 0.07[d] | 5.50 ± 0.18[d] |
| 3DRP | 0 | 3.47 ± 0.06[b] | | 7.53 ± 0.55[c] | |
| | 8 | 3.10 ± 0.14[c] | 2.99 ± 0.16[c] | 8.06 ± 0.96[d] | 6.88 ± 0.39[d] |
| | 16 | 3.60 ± 0.14[c] | 3.52 ± 0.09[c] | 6.98 ± 0.35[d] | 7.26 ± 0.45[d] |

PET, positron emission tomography; OESEM, ordered subsets expectation maximum; MAP, maximum *a posteriori*; 3DRP, three-dimensional filtered backprojection.

[a] Data are mean values and corresponding standard errors.

[b] Number of measurements = 20.

[c] Number of measurements = 10.

[d] Number of measurements = 5.

the measured FWHM for 3DRP was worse than for the iterative techniques by 0.3–0.7 mm for $^{18}$F and 0.5–1.3 mm for $^{124}$I.

Figure 3 presents results from the response linearity study. The data show good linearity over a range of activity concentrations relevant to microPET imaging for both $^{18}$F and $^{124}$I and for both OSEM and MAP reconstruction. Average recovery (image/true) of true activity concentrations for $^{18}$F was approximately 96% for MAP and 79% for OSEM, consistent with the better off-axis spatial resolution obtained with MAP (Table 1). As expected, due to the greater $\beta^+$ range, activity concentration recovery was clearly poorer for $^{124}$I (average 68% for MAP, 57% for OSEM) than for $^{18}$F ($p < 0.02$ by the paired-sample *t* test).

The effect of true-coincidence $\gamma$-ray background is clearly seen in Figure 4. Background counts outside the image of the contrast phantom are comprised of scatter events and, in the case of $^{124}$I, true-coincidence $\gamma$-ray background events. The scatter component should have been approximately the same for the two radionuclides, implying that the higher background level for $^{124}$I is due to true-coincidence $\gamma$-ray background events. Note, however, that the signal-to-background ratio is still greater than 20:1 for $^{124}$I. For $^{18}$F, the amplitude of the background decreases toward the edges of the field of view (FOV), whereas for $^{124}$I the level is almost constant across the entire FOV. This presumably reflects the fact that the cascade $\gamma$ rays are emitted isotropically relative to the directions of the corresponding annihilation photons, and thus, that the true-coincidence $\gamma$-ray background is spatially random in nature. On the other hand, the likelihood of a scatter event (i.e., an event in which one or both annihilation photons from a given $\beta^+$ decay are diverted from their initial directions prior to detection) decreases with increasing angle of scatter, implying that scatter background declines with increasing distance from the radioactive source. Figure 4 shows that, for a phantom approximating the size and shape of a mouse, true-coincidence $\gamma$-ray background events dominate the background counts for $^{124}$I.

Figure 4 also compares image contrast for $^{124}$I and $^{18}$F. For $^{18}$F, the appearance of counts in the cold region is caused by the limited spatial resolution of the reconstructed images and by scatter events from the surrounding activity. The con-

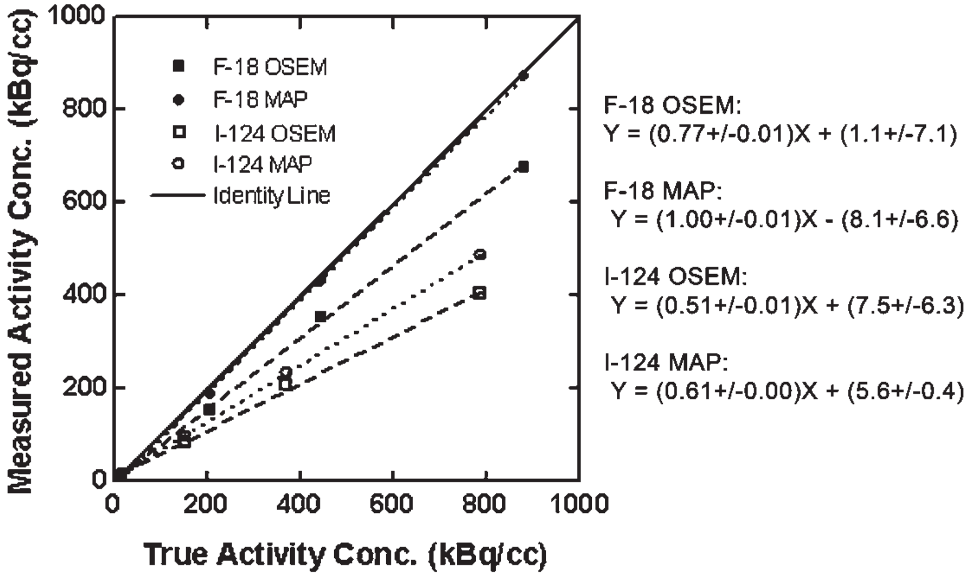

**Figure 3.** Positron emission tomography (PET) activity concentration response for $^{18}$F and $^{124}$I, using ordered subsets expectation maximum and maximum *a posteriori* reconstruction methods. The plot shows image-derived versus true activity concentration from PET scans of the linearity phantom filled with activity concentrations spanning the range of tissue-activity concentrations seen in the mouse antibody scans. Broken lines represent least-squares linear fits; equations and parameter standard deviations for the regression lines are shown on the right. For each syringe, a volume of interest (VOI) was created that contained the four hottest adjacent voxels in each of 25–40 slices. The average voxel value within each VOI was multiplied with the cylindrical phantom-based calibration factor appropriate to the radionuclide and reconstruction algorithm, and the resulting image-derived activity concentrations were plotted versus the measured values.

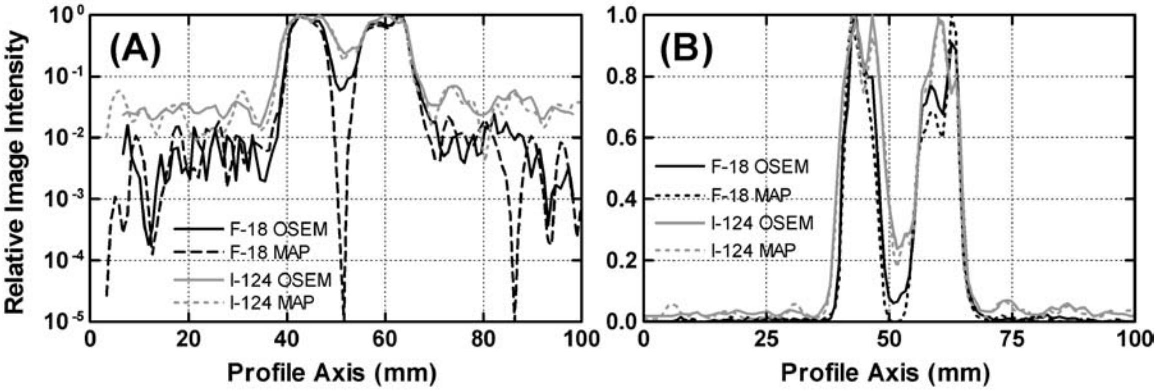

**Figure 4.** Normalized image intensity profiles through images of the contrast phantom (Fig. 1) demonstrating hot-to-cold image contrast and how the background obtained with $^{124}$I differs in shape and level from that with $^{18}$F. Profile windows (six transaxial slices wide) were placed in a coronal slice through the cold insert, and a mean profile was computed. The resulting profiles were normalized to a common maximum and plotted for comparison. (**A**) Semilog plot. (**B**) Linear plot.

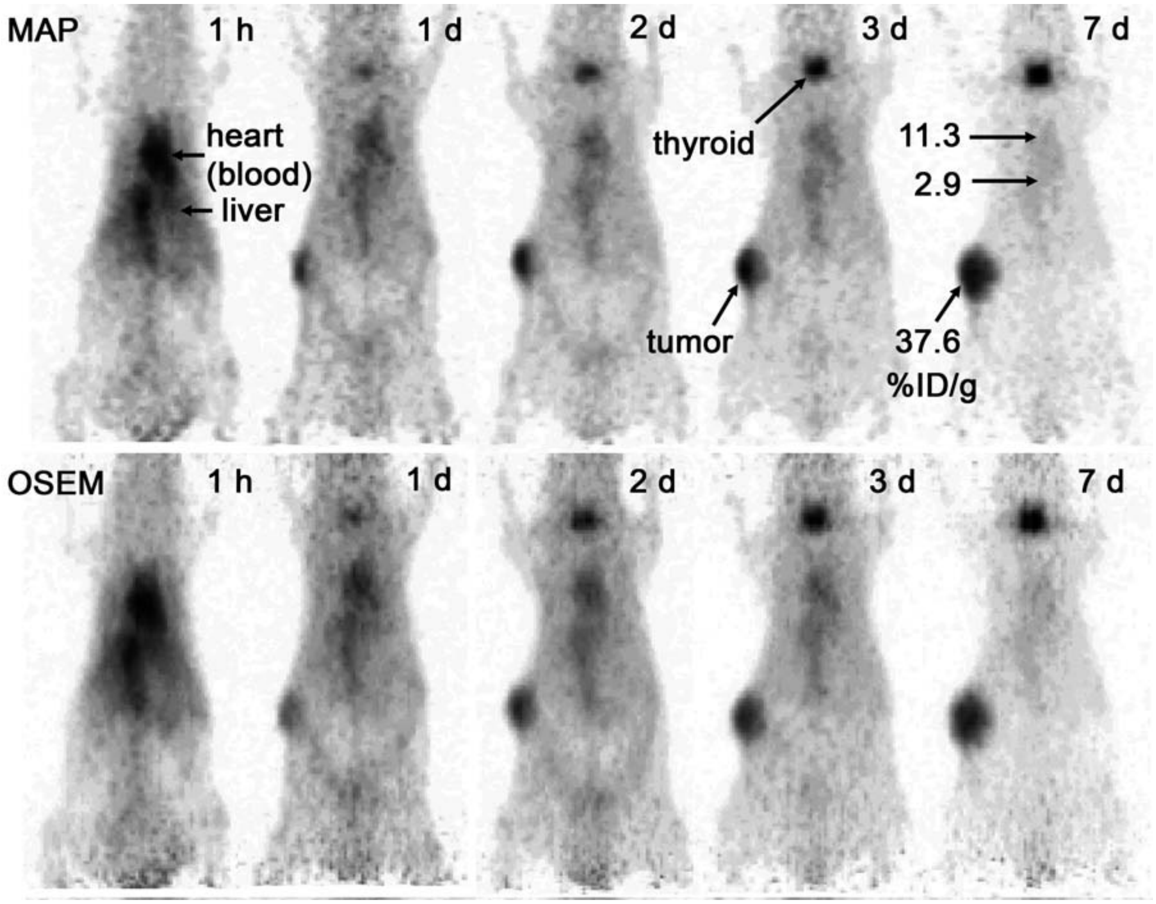

**Figure 5.** Maximum intensity projection (MIP) images of a nude mouse implanted in the right flank with a human colon tumor (LS-174T). Images were reconstructed with maximum *a posteriori* (MAP) (top row) and ordered subsets expectation maximization (OSEM) (bottom row) algorithms and normalized to reflect decay-corrected relative image intensities at the various times of scan. Uptake values (percentage of injected dose/g of tissue), measured by direct tissue assay, are indicated on the Day 7 MAP image. The tumor weighed 190 mg at the time of sacrifice following the final scan. In part, the apparent enlargement of the tumor images with time reflects tumor growth over the course of the experiment.

trast is lower for $^{124}$I due to the combined effects of the true-coincidence $\gamma$-ray background and longer $\beta^+$ range. The differences in background and contrast between OSEM and MAP reconstruction are modest, except for the dramatic minimum at the center of the cold region in the $^{18}$F MAP reconstruction. The presence of similar minima at symmetric locations on both sides of the one in the middle (Fig. 4A) suggests an artifact in the MAP reconstruction.

Serial images of a tumor-bearing mouse injected with [$^{124}$I]cT84.66 mAb are shown in Figure 5. Image resolution and contrast appear modestly improved with MAP, compared with OSEM reconstruction. The tumor was well visualized by 1 day postinjection, and tumor-to-nontumor contrast continued to increase through Day 7. Antibody deiodination, as judged from the percentage of total image counts observed in the thyroid, appears to have been modest, in spite of the fact that no effort was made to block iodine accumulation in the thyroid. Decay-corrected TACs-derived from the serial microPET scans are plotted in Figure 6.

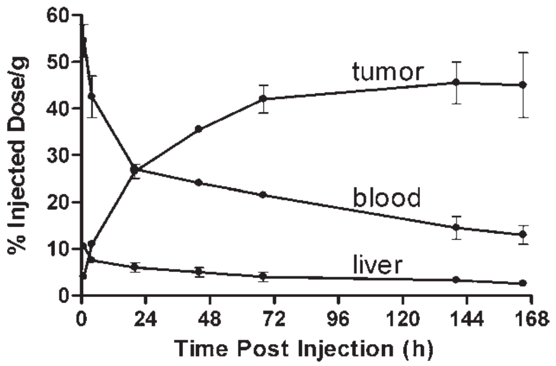

**Figure 6.** Image-derived, decay-corrected time-activity curves (TACs). Data are the mean ± standard error of the mean for 2 mice injected with $^{124}$I cT84.66 monoclonal antibody; the tumor weights at sacrifice on Days 7 were 40 and 190 mg. TAC shapes were determined from relative image intensities in serial positron emission tomography (PET) scans, whereas TAC amplitudes were normalized to agree with direct tissue assays performed postsacrifice after the final microPET scan. For some data points, the error bars are too small to be distinguished from the symbols representing the mean values.

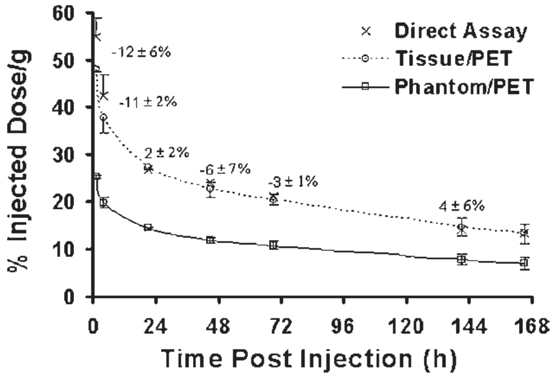

**Figure 7.** Image-derived estimates of $^{124}$I activity concentration in the blood, compared with direct venous samples. Data were corrected for $^{124}$I decay and averaged for 2 mice; each direct-assay data point is an average of samples taken just prior to, and just after, imaging. Phantom/positron emission tomography (PET) and Tissue/PET are microPET time-activity curves for heart calibrated, respectively, by imaging a known mouse phantom (24-cc vial) or normalizing to blood samples at the final time point. (Note that, by definition, direct-assay and Tissue/PET data agree at the final time point.) Mean errors (±standard error of the mean; $n = 2$) for Tissue/PET calibration are indicated. Clearly, Tissue/PET calibration was superior to Phantom/PET calibration.

Data validating microPET quantitation, using image-to-direct-tissue assay calibration, are presented in Figure 7. Image intensities determined for the heart on Day 7 were normalized to activity concentrations in blood measured from a 0.2-cc sample drawn by trans-thorax needle aspiration immediately after the scan and before the sacrifice. (Calibration factor = blood-activity concentration/image intensity for the heart at the last time point.) Blood-activity concentrations determined by tail prick on Day 7 differed by less than 2% from the values obtained with the cardiac samples. The plots in Figure 7 demonstrate a positive agreement between direct blood samples taken by tail prick before and after each scan and the normalized PET data. Differences [100(image/direct assay − 1)] were −12 ± 6% (mean ± standard error of the mean) at 1 hour, −11 ± 2% at 4 hours, and less than 6% in magnitude with varying signs at later time points. The underestimates at the earliest time points are likely due to larger background contributions to the heart images relative to signal from blood activity as time increased, resulting in an underestimation of the true calibration factors.

The use of a single calibration factor obtained by scanning a uniform cylinder phantom approximating the size of a mouse body failed to produce accurate estimates of tissue $^{124}$I activity concentration, an observation that is consistent with the response linearity study (Fig. 3). Errors obtained with this method for the 2 mice given [$^{124}$I]cT84.66 are shown in Table 2.

**Table 2.** MicroPET Activity Concentration Measurement Results Using Phantom-Based Calibration

| | | *% Error* | |
|---|---|---|---|
| *Tissue or organ* | *Time postinjection* | *Mouse 1* | *Mouse 2* |
| Blood | 1 hour to 7 days | −44 to −58 | −45 to −52 |
| Liver | 7 days | 7 | −20 |
| Tumor (190 mg) | 7 days | −46 | — |
| Tumor (40 mg) | 7 days | — | −66 |

PET, positron emission tomography.

[a] % error = 100(microPET − direct assay)/direct assay.

## DISCUSSION

The primary finding in this study was that, in spite of the drawbacks in the radionuclide's physical decay scheme, good (i.e., only modestly degraded) image quality and usefully accurate measurements of the biodistribution of a tumor-targeted, intact mAb can be obtained with $^{124}$I and small-animal PET, using the same scanning and image-reconstruction techniques routinely employed with $^{18}$F. Tumor, heart, large central vessels, and thyroid were all clearly identifiable in the images. When images were calibrated to match the activity concentration of the final blood sample on Day 7, the time-activity curves obtained from images of the heart agreed with parallel blood samples within 12% at all time points and within 6% at 1 day and later. It has been shown in studies with $^{64}$Cu-labeled anti-CEA mAbs that TACs obtained with microPET and this calibration method produce good agreement with TACs measured for tumor, liver, and blood in separate, parallel groups of mice by direct tissue assay.[24]

Of the two anticipated problems for $^{124}$I, high $\beta^+$ energy, and true-coincidence $\gamma$-ray background, the former appears to be the more significant. The positron-range effect can be modeled in iterative reconstruction, and some work has been done on this for MAP.[25] Clearly, such a correction could have a highly beneficial effect on small-animal PET image resolution (Fig. 2 and Table 1) and quantification for $^{124}$I (compare the activity recovery for $^{124}$I and $^{18}$F in Fig. 3). True-coincidence $\gamma$-ray background was apparently small relative to the true annihilation photon coincidence signal (Fig. 4). While it may have contributed to the increasing errors in the earlier time points of the image-derived blood TACs of Figure 7, the quantitative effects of true-coincidence $\gamma$-ray background in $^{124}$I imaging of mice are clearly small. (Note, however, that the problem is likely to worsen in larger animals, such as rats.) One additional, indirect effect of the true-coincidence $\gamma$-ray background is that it obviates the use of the standard scatter correction for the microPET scanner. That correction is based on a model of the shape of the scatter profile and, as seen in Figure 4, the combined scatter and true-coincidence $\gamma$-ray background for $^{124}$I has a very different shape from that of a pure $\beta^+$ emitter such as $^{18}$F.

It may be that true-coincidence $\gamma$-ray background for $^{124}$I can be significantly decreased by reducing the width of the microPET energy window. After seeing relatively little effect on image quality in a preliminary trial, the investigators decided that the potential improvement did not warrant the effort required to renormalize the scanner for use with the altered window.

One source of error in the current *in vivo* study that potentially affects all multiday imaging and biodistribution studies in tumor-bearing mice is tumor growth during the course of the experiment. In general, radiopharmaceutical uptake per unit of tissue weight tends to be inversely related to tumor size due to decreasing perfusion of the central region as the tumor grows. Tumor growth and different tumor sizes for Mouse 1 (tumor weight, 190 mg on Day 7) and Mouse 2 (tumor weight, 40 mg on Day 7) may have contributed to the increasing error bars and decreasing slope of the average tumor TAC with increasing time postinjection (Fig. 6). An empirical correction for the dependence of anti-CEA mAb uptake per gram on tumor size has been developed,[26,27] but its application requires a reliable method for measuring tumor size over the course of the dynamic experiment.[28]

A logical application of quantitative, serial small-animal PET with $^{124}$I is to determine TACs and tissue/organ cumulated activities in mouse models for use in the development of new radioimmunotherapy agents labeled with radioiodine ($^{131}$I, $^{125}$I). Clearly, $^{124}$I microPET is capable of delivering the needed time-activity data.

## CONCLUSIONS

Long $\beta^+$ range and true-coincidence $\gamma$-ray background notwithstanding, accurate biodistribution measurements can be obtained from tumor-bearing mice by using $^{124}$I anti-CEA mAbs with standard microPET acquisition and processing techniques. Thus, $^{124}$I may be effective as an imaging surrogate for other radioisotopes of iodine (i.e., $^{125}$I and $^{131}$I) used for targeted, internally administered radiation therapy.

Tissue- and organ-specific calibration of microPET images implicitly corrects for errors, such as partial volume effects, background counts, and tissue attenuation. It provides a simple, effective technique for obtaining quantitative accuracy in mouse models with microPET, and, at least for $^{124}$I, clearly outperforms calibration based on a cylindrical phantom approximating the size of a mouse body.

## ACKNOWLEDGMENTS

The cT84.66 mAb used in this study was prepared by Anne-Line Anderson. Desiree Crow prepared the xenografted mice and injected them with $^{124}$I mAb. Financial support for the study was provided by National Institutes of Health (Bethesda, MD) grant CA-P01-043904. SES was on sabbatical leave and supported by grants from the Swedish Research Council and the Swedish Cancer Foundation.

## REFERENCES

1. Koral KF, Dewaraja Y, Li J, et al. Update on hybrid conjugate-view SPECT tumor dosimetry and response in $^{131}$I-tositumomab therapy of previously untreated lymphoma patients. *J Nucl Med* 2003;44:457.
2. DeNardo GL, Kennel SJ, Siegel JA, et al. Radiometals as payloads for radioimmunotherapy for lymphoma. *Clin Lymphoma* 2004;5(Suppl. 1):S5.
3. Dewaraja YK, Kaminski M, Wilderman SJ, et al. Initial results for 3D patient-specific dosimetry in I-131 tositumab using dual-modality SPECT/CT imaging at multiple times of patients with follicular lymphoma. *J Nucl Med* 2006;47(Suppl. 1):156P.
4. Dillman LT, Von der Lage FC. *NM/MIRD Pamphlet No. 10: Radionuclide Decay Schemes and Nuclear Parameters for Use in Radiation-Dose Estimation*. New York. Society of Nuclear Medicine, 1975:69.
5. Koppe MJ, Bleichrodt RP, Oyen WJ, et al. Radioimmunotherapy and colorectal cancer. *Br J Surg* 2005;92:264.
6. Bryan JN, Jia F, Mohsin H, et al. Comparative uptakes and biodistributions of internalizing vs. noninternalizing copper-64 radioimmunoconjugates in cell and animal models of colon cancer. *Nucl Med Biol* 2005;32:851.
7. Bakir MA, Eccles S, Babich JW, et al. c-erbB2 protein overexpression in breast cancer as a target for PET using iodine-124-labeled monoclonal antibodies. *J Nucl Med* 1992;33:2154.
8. Lee FT, Hall C, Rigopoulos A, et al. Immuno-PET of human colon xenograft-bearing BALB/c nude mice using $^{124}$I-CDR-grafted humanized A33 monoclonal antibody. *J Nucl Med* 2001;42:764.
9. Robinson MK, Doss M, Shaller C, et al. Quantitative immuno-positron emission tomography imaging of HER2-positive tumor xenografts with an iodine-124 labeled anti-HER2 diabody. *Cancer Res* 2005;65:1471.
10. Collingridge DR, Carroll VA, Glaser M, et al. The development of [(124)I]iodinated-VG76e: A novel tracer for imaging vascular endothelial growth factor *in vivo* using positron emission tomography. *Cancer Res* 2002; 62:5912.
11. Fortin MA, Salnikov AV, Nestor M, et al. Immuno-PET of undifferentiated thyroid carcinoma with radioiodine-labelled antibody cMAb U36: Application to antibody tumour uptake studies. *Eur J Nucl Med Mol Imaging* 2007;34:1376.
12. Sundaresan G, Yazaki PJ, Shively JE, et al. $^{124}$I-labeled engineered anti-CEA minibodies and diabodies allow high-contrast, antigen-specific small-animal PET imaging of xenografts in athymic mice. *J Nucl Med* 2003; 44:1962.
13. Laforest R, Rowland DJ, Welch MJ. MicroPET imaging with nonconventional isotopes. *IEEE Trans Nucl Sci* 2002;49:2119.
14. Yao R, Balakrishnan S, Ambwani S, et al. Quantitative iodine-124 imaging on animal PET. *Nucl Sci Symp Conf Record, 2005 IEEE* 2005;3:4.
15. Pal A, Glekas A, Doubrovin M, et al. Molecular imaging of EGFR kinase activity in tumors with $^{124}$I-labeled small molecular tracer and positron emission tomography. *Mol Imaging Biol* 2006;8:262.
16. Zanzonico P, O'Donoghue J, Chapman JD, et al. Iodine-124-labeled iodo-azomycin-galactoside imaging of tumor hypoxia in mice with serial microPET scanning. *Eur J Nucl Med Mol Imaging* 2004;31:117.
17. Hefta LJF, Neumaier M, Shively JE. Kinetic and affinity constants of epitope specific anti-carcinoembryonic antigen (CEA) monoclonal antibodies for CEA and en-

gineered CEA domain constructs. *Immunotechnology* 1998;4:49.

18. Neumaier M, Shively L, Chen FS, et al. Cloning of the genes for T84.66, an antibody that has a high specificity and affinity for carcinoembryonic antigen, and expression of chimeric human/mouse T84.66 genes in myeloma and Chinese hamster ovary cells. *Cancer Res* 1990;50:2128.
19. Fraker PJ, Speck JC, Jr. Protein and cell membrane iodinations with a sparingly soluble chloroamide, 1,3,4,6-tetrachloro-3a,6a-diphrenylglycoluril. *Biochem Biophys Res Commun* 1978;80:849.
20. Knoess C, Siegel S, Smith A, et al. Performance evaluation of the microPET R4 PET scanner for rodents. *Eur J Nucl Med Mol Imaging* 2003;30:737.
21. Shepp LA, Vardi Y. Maximum likelihood reconstruction for emission tomography. *IEEE Trans Med Imaging* 1982;MI-2:113.
22. Ruangma A, Laforest R, Bing B, et al. Characterization of USC-MAP image reconstruction on microPET-R4. *Nucl Sci Symp Conf Record, 2004 IEEE* 2004;6:3449.
23. Kinahan P, Rogers J. Analytic 3D image reconstruction using all detected image events. *IEEE Trans Nucl Sci* 1989;36:964.
24. Li L, Bading JR, Yazaki PJ, et al. A versatile bifunctional chelate for radiolabeling humanized anti-CEA antibody with In-111 and Cu-64 at either thiol or amino groups: PET imaging of CEA-positive tumors with whole antibodies. *Bioconju Chem* 2008;19:89.
25. Ruangma A, Bai B, Lewis JS, et al. Three-dimensional maximum a posteriori (MAP) imaging with radiopharmaceuticals labeled with three Cu radionuclides. *Nucl Med Biol* 2006;33:217.
26. Williams LE, Duda RB, Proffitt RT, et al. Tumor uptake as a function of tumor mass: A mathematic model. *J Nucl Med* 1988;29:103.
27. Ferl GZ, Wu AM, DiStefano JJ, 3rd. A predictive model of therapeutic monoclonal antibody dynamics and regulation by the neonatal Fc receptor (FcRn). *Ann Biomed Eng* 2005;33:1640.
28. Bading J, Williams L, Colcher D, et al. Methods for clarifying the interpretation of antibody kinetic studies in tumor-bearing mice. *Radiopharmaceuticals* 2006;21:399.